IAEA nuclear fusion

Estimating cross-field particle transport at the outer midplane of TCV by tracking filaments with machine learning

OPEN ACCESS
IOP Publishing | International Atomic Energy Agency

Nuclear Fusion

Nucl. Fusion **63** (2023) 076025 (10pp)

https://doi.org/10.1088/1741-4326/acdae5

Estimating cross-field particle transport at the outer midplane of TCV by tracking filaments with machine learning

W. Han[1,*], N. Offeddu[2], T. Golfinopoulos[1], C. Theiler[2], J.L. Terry[1], C. Wüthrich[2], D. Galassi[2], C. Colandrea[2], E.S. Marmar[1] and the TCV Team[2,a]

[1] MIT Plasma Science and Fusion Center, Cambridge, MA 02139, United States of America
[2] École Polytechnique Fédérale de Lausanne (EPFL), Swiss Plasma Center (SPC), CH-1015 Lausanne, Switzerland

E-mail: harryhan@mit.edu

Received 23 December 2022, revised 12 May 2023
Accepted for publication 2 June 2023
Published 9 June 2023

CrossMark

Abstract

Cross-field transport of particles in the boundary region of magnetically confined fusion plasmas is dominated by turbulence. Blobs, intermittent turbulent structures with large amplitude and a filamentary shape appearing in the scrape-off layer (SOL), are known from theoretical and experimental studies to be the main contributor to the cross-field particle transport. The dynamics of blobs differs depending on various plasma conditions, including triangularity (δ). In this work, we analyze triangularity dependence of the cross-field particle transport at the outer midplane of plasmas with $\delta = +0.38$, $+0.15$, -0.14, and -0.26 on the Tokamak à Configuration Variable, using our novel machine learning (ML) blob-tracking approach applied to gas puff imaging data. The cross-field particle flux determined in this way is of the same order as the overall transport inferred from KN1D, GBS, and SOLPS-ITER simulations, suggesting that the blobs identified by the ML blob-tracking account for most of the cross-field particle transport in the SOL. Also, the ML blob-tracking and KN1D show a decrease in the cross-field particle transport as δ becomes more negative. The blob-by-blob analysis of the result from the tracking reveals that the decrease of cross-field particle transport with decreasing δ is accompanied by a decrease in the number of blobs in a fixed time, which tend to have larger area and lower radial speed. Also, the blobs in these plasmas are in the connected sheath regime, and show a velocity scaling consistent with the two-region model.

Keywords: negative triangularity, edge/SOL turbulence, machine learning, gas puff imaging, particle transport, tokamak

(Some figures may appear in colour only in the online journal)

[a] See Reimerdes *et al* 2022 (https://doi.org/10.1088/1741-4326/ac369b) for the TCV Team.
[*] Author to whom any correspondence should be addressed.

1. Introduction

Particle transport in magnetically confined fusion plasmas is a critical factor constraining reactor performance, determining confinement, impurity content, wall loading, and fueling and detachment requirements. Plasma turbulence in the boundary region has been known to be the major cause of the particle transport in the edge, as demonstrated in theoretical studies [1] and experiments [2]. Specifically, intermittent turbulence with large amplitude, filamentary structures (elongated along the field) in the scrape-off layer (SOL) [3–5], called blobs, plays a key role in the cross-field particle transport [2, 5–8]. Filamentary turbulence differs depending on various plasma conditions, including core density [9, 10], and plasma shape, e.g. the triangularity (δ) [11]. Compared to the conventional positive δ plasmas, negative δ plasmas have been shown to exhibit reduced core fluctuations [12–14] as well as edge/SOL fluctuations [11]. Previous work [11] has demonstrated that first-wall interaction can be completely suppressed for L-mode plasmas with $\delta \lesssim -0.25$ on the Tokamak à Configuration Variable (TCV), an effect ascribed to blobs becoming discharged by the short connection length.

Here, we extend the results of [11] to the study of cross-field particle transport at the outer midplane of negative triangularity plasmas, and explore the role of blobs in cross-field particle transport. There can be a poloidal dependence of the cross-field particle transport, but this is not addressed in this analysis. In particular, the contribution of blobs of different sizes to the cross-field particle transport is investigated, as they belong to different turbulent regimes depending on their sizes [7, 15]. To obtain the distribution of blob sizes, we use gas puff imaging (GPI) data with our newly developed machine learning (ML) model for blob-tracking [16, 17], which tracks the shapes and trajectories of individual blobs frame-by-frame. We used the ML blob-tracking to estimate the cross-field particle transport, assuming that the light emission in the GPI data corresponds to the radial convective motion, and that the far-SOL transport is essentially convective, not diffusive [18]. We find that cross-field particle transport through the far-SOL at the outboard midplane, in a fiducial TCV plasma, as estimated by the ML blob-tracking, is of the same order as the flux evaluated by simulations of varying fidelity, specifically KN1D [19], GBS [20], and SOLPS-ITER [21]. Also, cross-field particle transport in plasmas with $\delta = +0.38, +0.15, -0.14$, and -0.26 are estimated using both ML blob-tracking and KN1D. Both results show a decrease in overall cross-field particle transport with decreasing δ. The analysis of the ML blob-tracking shows that plasmas with smaller δ tend to have less frequent blobs, most of which have larger area and lower radial speed, leading overall to a lower cross-field particle transport. Furthermore, as δ becomes more negative, the blob regime tends to be shifted toward the regime with a higher collisionality. This paper is structured as follows. Section 2 elaborates on how the blob-induced cross-field particle transport is estimated using the ML blob-tracking of the GPI data. Section 3 compares four different estimates of the cross-field particle transport in a fiducial TCV plasma, obtained using the ML blob-tracking of the experimental data, and modeling with KN1D, GBS, and SOLPS-ITER. It also shows the comparison of the cross-field particle transport for different δ values, as further investigated by the blob-by-blob analysis from the ML blob-tracking. The dynamic regime of the blobs are also analyzed with the individual blob information estimated by the tracking. Lastly, we present conclusions and remarks in section 4.

2. Background

2.1. GPI diagnostic on TCV

GPI diagnostics measure the edge/SOL fluctuations by imaging atomic emission from the excitation of a local neutral gas puff [22]. On TCV, nozzles installed near the outboard midplane puff D_2 gas[3] and 12×10 optical fibers view the light emission along lines-of-sight that are aligned to the local magnetic field [23]. The signals are transmitted through the optical fibers and onto avalanche photo-diodes (APD) through D_α (656 nm) filters, and recorded by digitizers with a sampling rate of 2 MHz. The location of the GPI views is displayed in figure 1(*a*) with the poloidal cross-section of a plasma in TCV. A snapshot of the GPI data capturing a blob on the right-hand side moving radially outward is shown in figure 1(*b*). The empty (white) spots correspond to GPI views with broken optical fibers.

2.2. ML model for blob-tracking in GPI images

The pattern recognition and tracking from images is a well-known task in ML, and has been implemented for blob-tracking in GPI data [17]. Four benchmarked models were trained with synthetic GPI data and two of the models show excellent performance on real GPI data, both in shape prediction and blob regime identification. An example of ML blob detection is shown in figure 1(*c*). The raw GPI brightness in figure 1(*b*) is standardized (i.e. mean-subtracted and divided by the standard deviation), interpolated to a denser grid, translated to a range $[0, a]$ where $a > 0$ is the same for all pixels, and scaled to the $[0, 1]$ range for the input of the ML blob-tracking. Note that this normalization scheme is used only for finding the boundary of the blob, which is identified as the blue contour in the figure.

ML blob-tracking can be used to estimate cross-field particle transport by blobs as follows. First, the local emissivity (ϵ) in the region of the neutral gas cloud is assumed to have a linear dependence on the local neutral density (n_n) and a non-linear dependence on the local electron density (n_e) and temperature (T_e), parameterized by [22, 24, 25]:

$$\epsilon \propto n_n n_e^{\alpha_n} T_e^{\alpha_T}. \tag{1}$$

Also, as the lines-of-sight of GPI are approximately aligned with the local magnetic field, the brightness (i.e. the

[3] He puff paired with He I (588 nm) filter is also available.

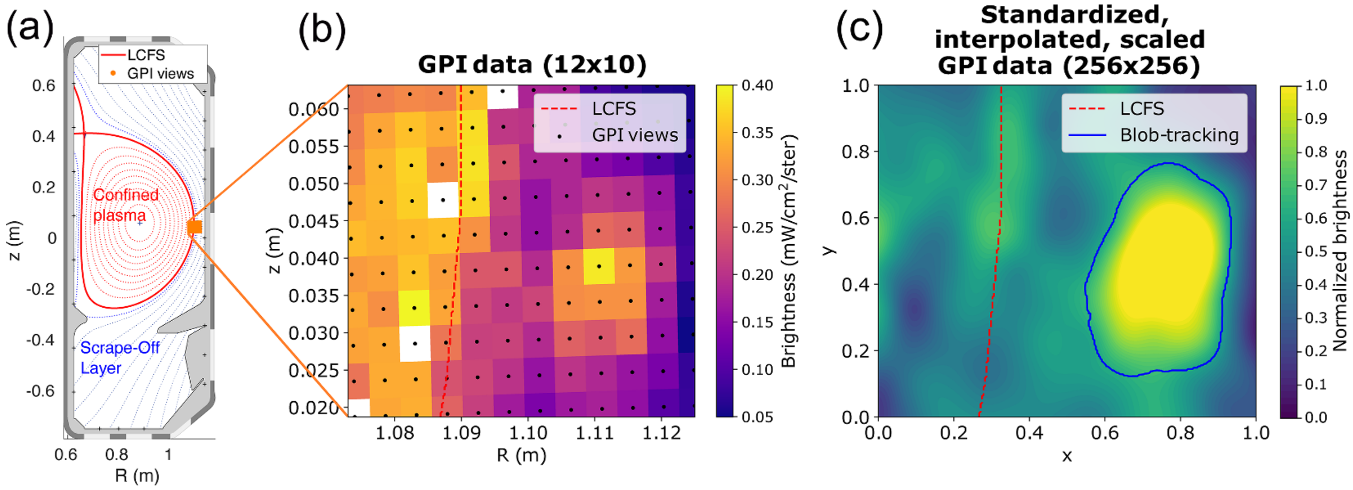

Figure 1. (*a*) Poloidal cross-section of a plasma in TCV with the locations of the 12×10 GPI views near the last closed flux surface (LCFS). Reproduced from [17]. CC BY 4.0. (*b*) Snapshot of the GPI brightness data capturing a blob in the far-SOL moving radially outward. Here, empty (white) spots correspond to GPI views with broken optical fibers. (*c*) The standardized GPI brightness (i.e. mean-subtracted and divided by the standard deviation) is interpolated to a denser grid (256×256), translated to a range $[0, a]$ where $a > 0$ is the same for all pixels, and scaled to the [0, 1] range. The boundary of the blob identified by the ML is shown by the blue contour.

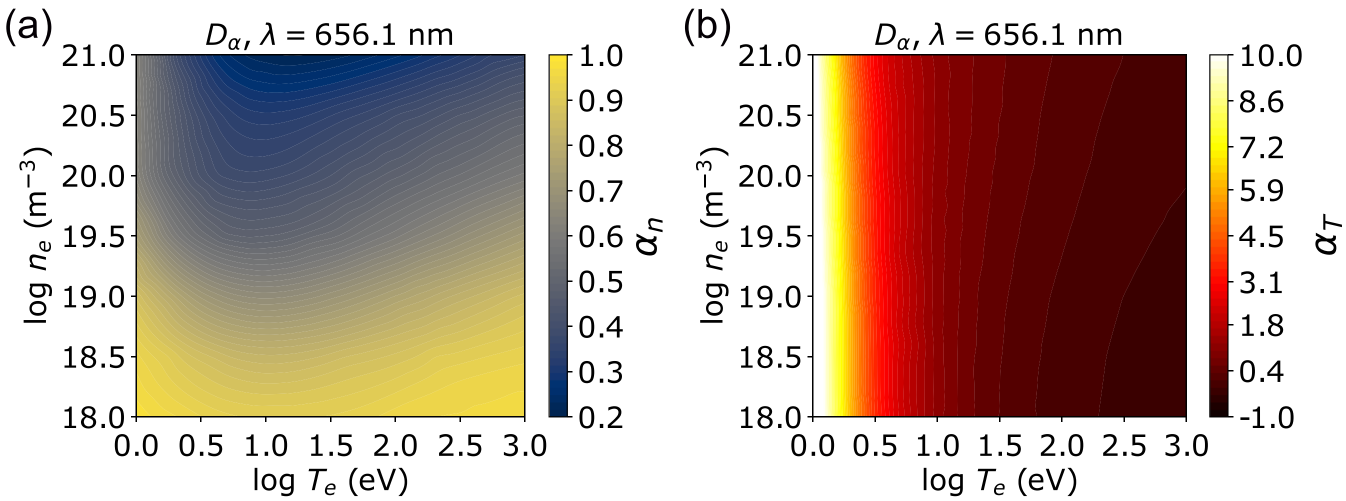

Figure 2. (*a*) Exponent α_n and (*b*) α_T in equation (2) computed for the D_α brightness from the DEGAS 2 code by Cziegler [24], as a function of $\log n_e$ and $\log T_e$.

line-integrated emissivity along the line-of-sight) (I) is expressed as:

$$I = A n_n n_e^{\alpha_n} T_e^{\alpha_T}, \tag{2}$$

where A is a proportionality factor which includes the toroidal extent of the gas cloud. The variation of n_e is much faster than that of n_n, so that the neutral density can be assumed to be constant over the time scale of interest [25]. The exponents α_n and α_T for the D_α brightness were computed from the DEGAS 2 code by Cziegler [24], for a range of n_e and T_e, as shown in figure 2. The brightness fluctuation ($\tilde{I}$) can then be approximated and linearized as follows [24]:

$$\tilde{I} = I - I_0 \tag{3}$$

$$= A n_n [n_e^{\alpha_n} T_e^{\alpha_T} - n_{e0}^{\alpha_n} T_{e0}^{\alpha_T}] \tag{4}$$

$$\approx A n_n \left[n_{e0}^{\alpha_n} T_{e0}^{\alpha_T} \left(\alpha_n \frac{\tilde{n}_e}{n_{e0}} + \alpha_T \frac{\tilde{T}_e}{T_{e0}} \right) \right], \tag{5}$$

where I_0, n_{e0}, and T_{e0} are the time averages of I, n_e, and T_e, respectively. This gives the expression for normalized brightness fluctuations:

$$\frac{\tilde{I}}{I_0} = \alpha_n \frac{\tilde{n}_e}{n_{e0}} + \alpha_T \frac{\tilde{T}_e}{T_{e0}}. \tag{6}$$

For the plasma conditions used in this work (L-mode, with $\delta = +0.38, +0.15, -0.14$, and -0.26), the ratio α_T/α_n in the GPI field-of-view (FoV) is shown in figure 3, which was computed according to figure 2 with n_e and T_e measured from Thomson scattering and the reciprocating probe. This shows that $\alpha_T < \alpha_n$ at the separatrix and in the near-SOL, but α_T can become comparable or even larger than α_n in the far-SOL. In

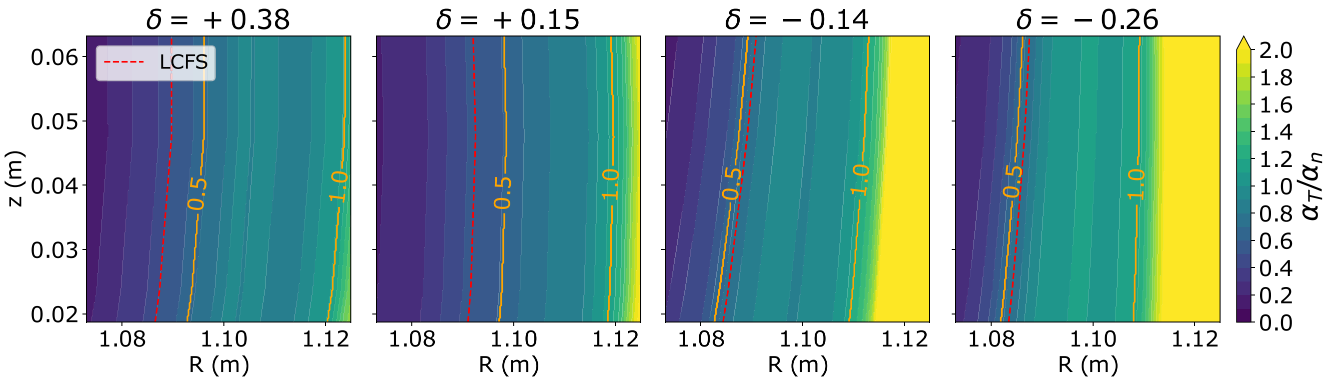

Figure 3. The ratio between the two exponents, α_T/α_n, in the GPI field-of-view for the plasmas used in this work ($\delta = +0.38$, $+0.15$, -0.14, and -0.26), computed according to figure 2 with n_e and T_e measured from Thomson scattering and the reciprocating probe (shot numbers: 65470, 65472).

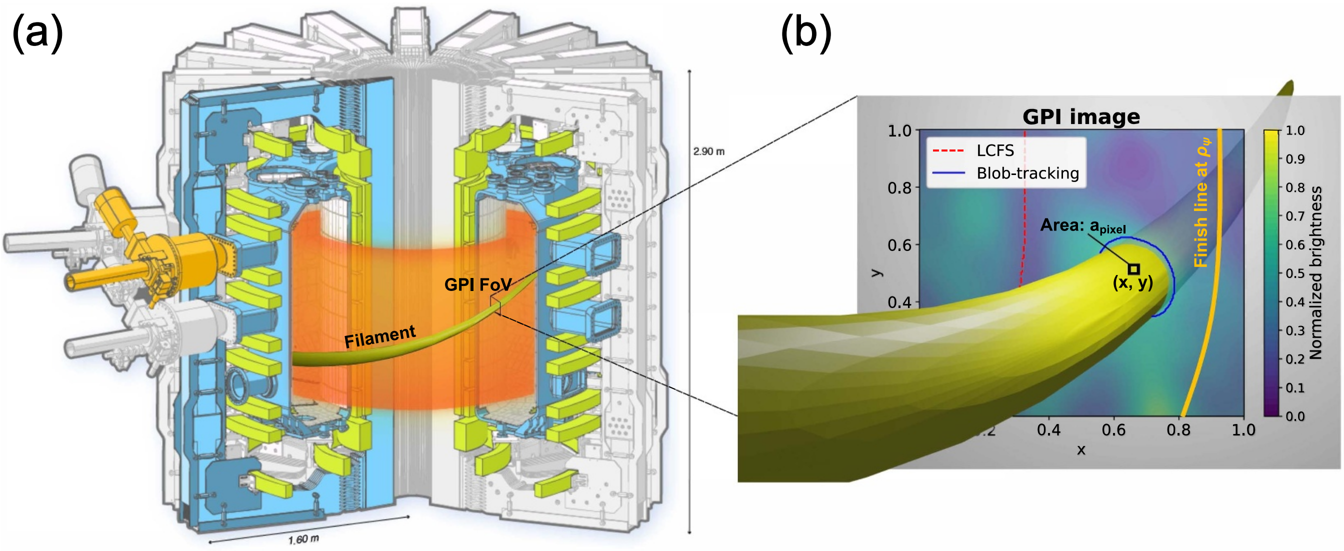

Figure 4. (*a*) Illustration of the three-dimensional structure of a turbulent filament (yellow object). Reproduced from [17]. CC BY 4.0. (*b*) Poloidal cross-section of the filament (i.e. the blob) in the GPI field-of-view. The boundary of the blob (blue solid line) is derived from the ML blob-tracking. A pixel at (x,y) inside the blob, having an area a_{pixel}, is denoted as a square; particles inside this pixel have a density fluctuation $\tilde{n}_e(x,y)$. Blobs are counted for the estimation of cross-field particle transport at ρ_ψ only if their center crosses the 'finish line' at ρ_ψ, shown as a solid orange line in the right panel. Credit for the TCV illustration on the left panel: EPFL.

this work, however, we assume $\alpha_n \frac{\tilde{n}_e}{n_{e0}} \gg \alpha_T \frac{\tilde{T}_e}{T_{e0}}$ and thus neglect the second term in the right-hand side of equation (6) [24, 26]. This gives us an upper-bound of $\tilde{n}_e$ if we assume $\tilde{n}_e$ and $\tilde{T}_e$ are in phase, with the caveat that $\tilde{n}_e$ may be overestimated in the far SOL. With $\tilde{I}$ and I_0 obtained from GPI, $\tilde{n}_e$ in a blob can then be computed for the group of pixels inside the blob's boundary found by ML blob-tracking (G_{blob}). Then the number of excess electrons per unit length orthogonal to the GPI FoV carried by a blob ($\tilde{\mu}_{e,\text{blob}}$ (m^{-1})) can be calculated by

$$\tilde{\mu}_{e,\text{blob}} = \sum_{(x,y)\in G_{\text{blob}}} \tilde{n}_e(x,y) a_{\text{pixel}}, \tag{7}$$

where a_{pixel} is the area of the pixel. Figure 4 illustrates the three-dimensional structure of a filament on the GPI image to aid understanding of the introduced quantities. Here, a fraction of the filament having a unit length orthogonal to the GPI FoV is considered.

In order to estimate the cross-field particle transport at the outboard midplane, at the radial location ρ_ψ, we count blobs whose center crosses a 'finish line' in the GPI FoV, where the 'finish line at ρ_ψ' is defined as the poloidal contour line of the ρ_ψ flux surface within the GPI FoV as shown in figure 4(*b*). Then the electron flux (i.e. the cross-field particle transport) due to all the blobs crossing the finish line at ρ_ψ, within the time window Δt, can be estimated by

$$\Gamma_{\text{blobs}}(\rho_\psi) = \sum_{i\in B_{\rho_\psi}} \langle \tilde{\mu}_{e,\text{blob},i}\rangle / \left(l_{fl}(\rho_\psi)\,\Delta t\right), \tag{8}$$

where $\langle \tilde{\mu}_{e,\text{blob},i}\rangle$ is the number of time-averaged excess electrons per unit length carried by blob i throughout its trajectory, B_{ρ_ψ} is the set of blobs crossing the finish line at ρ_ψ within the time window Δt, and $l_{fl}(\rho_\psi)$ is the length of the finish line at ρ_ψ in the GPI FoV. Toward smaller ρ_ψ, the profile of $\Gamma_{\text{blobs}}(\rho_\psi)$ is limited by the position of the LCFS and the average size of the blobs. There are not many blobs detected by the ML blob-tracking near the LCFS in the GPI images. If the gap between the LCFS and the finish line is small, few blobs are counted, leading to a bias in the estimate of the cross-field particle transport. Therefore, finish lines located near the LCFS (within the gap of an average blob size) are not considered. Also, at larger ρ_ψ, the profile of $\Gamma_{\text{blobs}}(\rho_\psi)$ is limited by the outermost edge of the GPI FoV and the average size of the blobs. When blobs touch the edge of the GPI FoV, the blob boundary is not closed, and the number of electrons carried by these blobs is underestimated. Thus, finish lines located near the outermost edge of the GPI FoV (again, within the gap of an average blob size) are also excluded from the analysis. With this approach we only account for transport due to sufficiently large blobs to be tracked by our fine resolution grid assuming they are the main radial transport mechanism in the far-SOL [2, 5–8, 18].

2.3. KN1D

KN1D is an algorithm which computes the particle transport for atomic and molecular hydrogen or deuterium in a 1D space of an ionizing plasma with specified plasma profiles as input [19]. Originally it is written in IDL. In this work, we ran KN1D in Python using Aurora, an open-source package for particle transport, neutrals and radiation modeling in magnetically confined fusion plasmas [27–29]. Neutral pressure, measured by a baratron gauge, is used as an input for KN1D, and uncertainty in the pressure measurement is one (but not the only) source of uncertainty in the resulting particle flux.

3. Results

3.1. Comparison of the results from simulations and tracking

The estimates of the cross-field particle transport computed from KN1D and the ML blob-tracking are compared with that found using two well-established simulation codes: GBS [20] and SOLPS-ITER [21], for an L-mode, lower-single null case (TCV-X21 reference case [30]) as shown in figure 5. All results give a similar level of cross-field particle flux, and this closeness reinforces the conclusion that the cross-field particle transport in the edge/SOL is indeed dominated by the blobs.

3.2. Cross-field particle transport in positive and negative triangularity plasmas

The plasmas presented in this section are ohmic-heated, inner-wall limited L-mode plasmas with $\delta = +0.38$, $+0.15$, -0.14, and -0.26 on TCV at a toroidal field $B_T = 1.4$ T and plasma current $I_p = 230$ kA. Plasma densities range from 3.8×10^{19} to 4.9×10^{19} m^{-3}, which correspond to Greenwald fractions of 0.27–0.37. GPI brightness from D_2 puffs was recorded and a data window of 40 ms was used for each of these plasmas, with Mask R-CNN for the blob-tracking [17]. The edge/SOL densities and temperatures were obtained from Thomson scattering and the reciprocating probe.

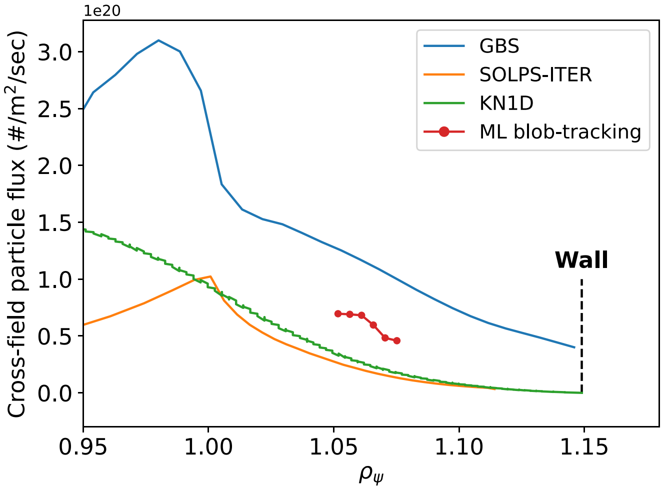

Figure 5. Cross-field particle flux as a function of ρ_ψ estimated from GBS, SOLPS-ITER, KN1D, and ML blob-tracking for the TCV-X21 reference case [30]. For GBS, the data is flux-averaged. For the other methods, the data is from the outer midplane. ρ_ψ at the outer-wall in the midplane is denoted as a dashed line.

Figure 6(*a*) displays the comparison of cross-field particle flux, as a function of ρ_ψ, between the $\delta = +0.38$, $+0.15$, -0.14, and -0.26 plasmas, estimated from KN1D (solid lines) and ML blob-tracking (solid lines with dots); average blob sizes are also evaluated and illustrated at the $\rho_\psi = 1.05$ surface. ρ_ψ at the outer wall is denoted by a dashed line for each plasma. These results further reinforce the validity of the ML blob-tracking method for the estimation of cross-field particle flux, giving values reasonably close to the results from KN1D. Additionally, the particle flux estimated by the reciprocating probe in the far-SOL of previous L-mode discharges in TCV, with similar plasma current and density, is also in the same order [31]. Furthermore, both KN1D and the ML blob-tracking show an overall similar trend with triangularity: $\delta = +0.38$ shows the highest flux, followed by $\delta = +0.15$, -0.14, and -0.26, although $\delta = -0.14$ and -0.26 are close in KN1D. Previously, it was observed that fluctuations were fully suppressed at the first wall, and in part of the SOL, for $\delta \lesssim -0.25$ [11]. The reduction in blob-induced transport indicated here in the $\delta = -0.26$ case, and even the partial reduction for outer flux surfaces at $\delta = -0.14$, is consistent with this earlier result. This phenomenon had been correlated to the drop-off in connection length occurring closer to the LCFS for more negative triangularities. However, this effect alone does not organize the observed reduction in transport from $\delta = +0.38$ through $\delta = +0.15$ to $\delta = -0.14$, since the connection lengths and blob sizes in these three cases are comparable. Additional, currently unidentified, mechanisms are needed to describe the difference between the positive and negative triangularity cases.

Further analysis of the contribution of blobs to the cross-field particle transport is shown in figure 7, which is a result that takes advantage of the ML blob-tracking algorithm's particular ability to compile information on individual blobs.

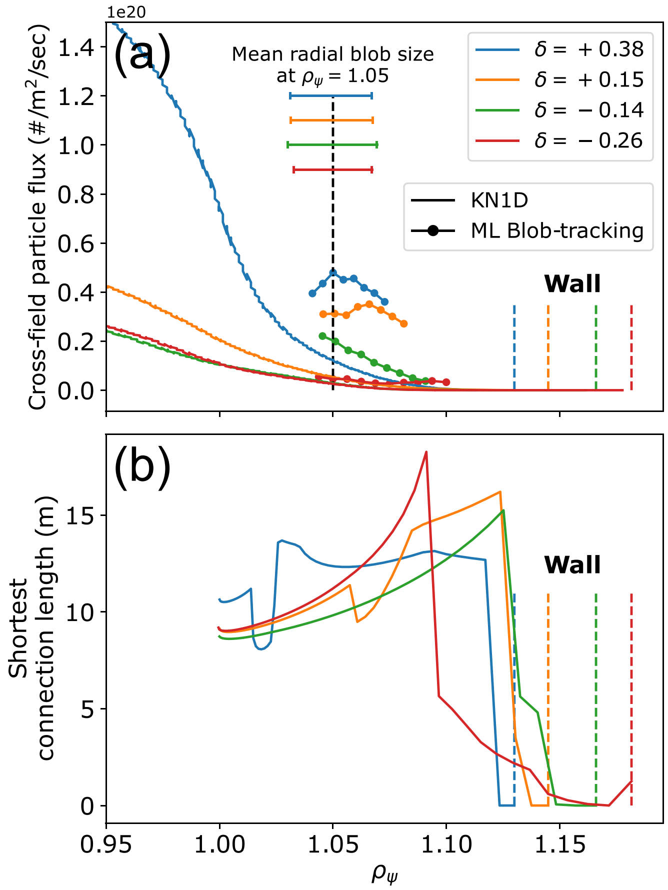

Figure 6. (*a*) Cross-field particle flux in the midplane estimated from KN1D (solid lines) and the ML blob-tracking (solid lines with dots), and (*b*) the shortest connection length to the target in the midplane computed from magnetic field reconstruction, as functions of ρ_ψ, for plasmas with $\delta = +0.38$, $+0.15$, -0.14, and -0.26 on TCV. ρ_ψ at the outer-wall in the midplane is denoted by dashed lines for each plasma. In the upper panel, the mean radial blob size (mapped onto the ρ_ψ coordinate) at $\rho_\psi = 1.05$ is indicated for each δ.

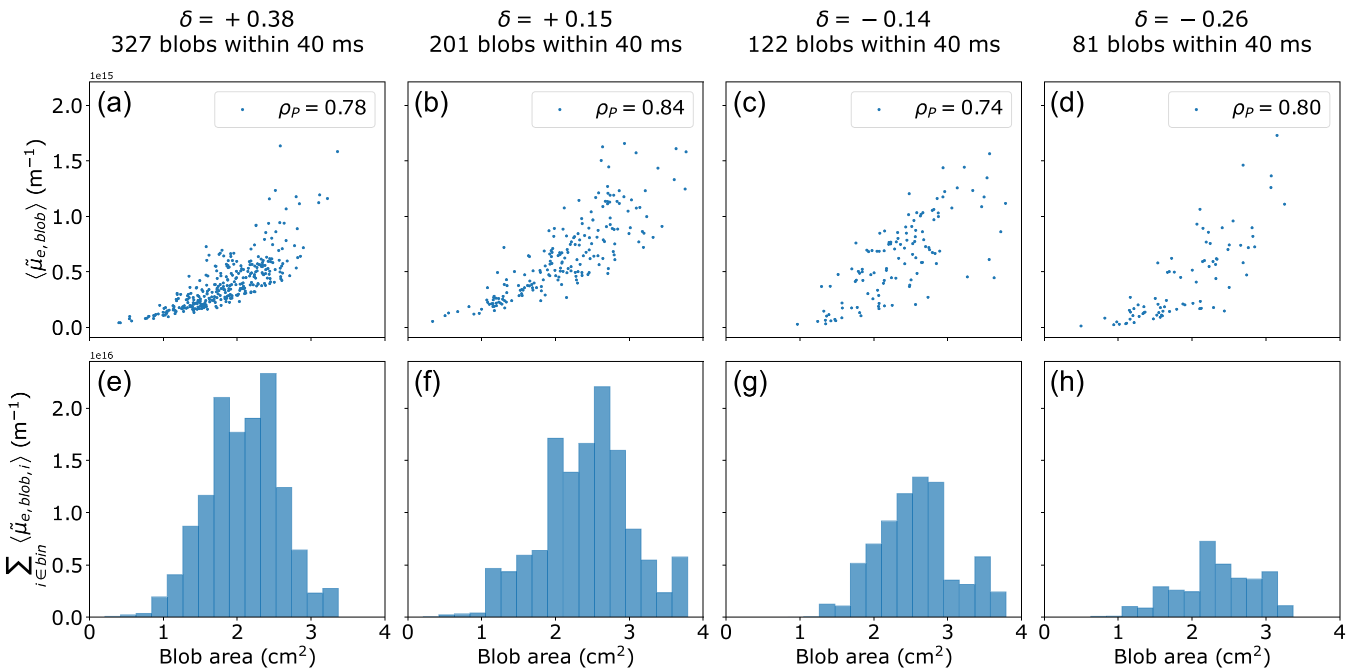

Figure 7. (*a*)–(*d*) The time-averaged number of excess electrons per unit length along the field line carried by individual blobs $\langle \tilde{\mu}_{e,\mathrm{blob}} \rangle$ (m^{-1}) with respect to their average area for plasmas with $\delta = +0.38$, $+0.15$, -0.14, and -0.26 on TCV. The Pearson correlation coefficient (ρ_P) is shown for each case. (*e*)–(*h*) The blob area is separated into equal sized bins and the bar length is the summation of data points contained in each bin.

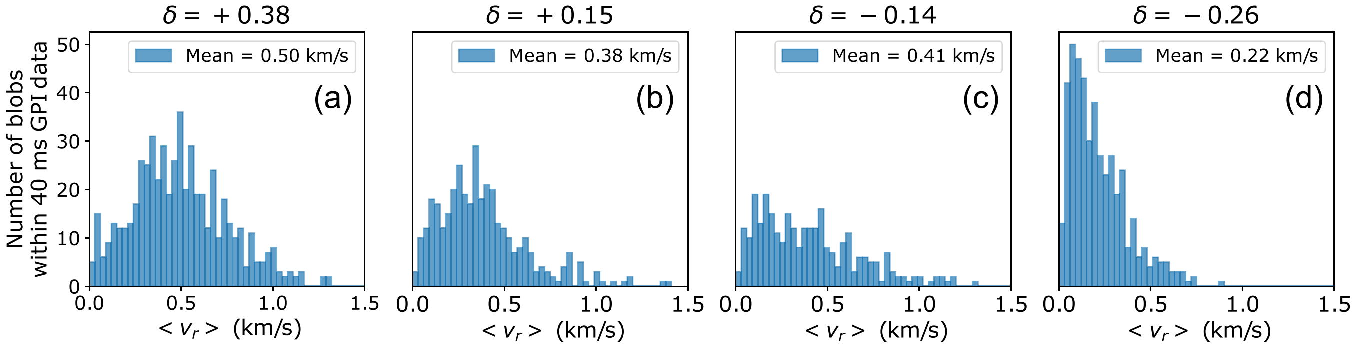

Figure 8. The histogram of the time-averaged radial speed $\langle v_r \rangle$ of all the blobs tracked within a 40 ms time window, for plasmas with $\delta = +0.38$, $+0.15$, -0.14, and -0.26 on TCV. The mean values are denoted for each case.

In figures 7(*a*)–(*d*), the time-averaged number of excess electrons per unit length along the field line, carried by individual blobs, $\langle \tilde{\mu}_{e,\text{blob}} \rangle$ (m^{-1}), is plotted as a function of their average area, for plasmas with $\delta = +0.38$, $+0.15$, -0.14, and -0.26. The Pearson correlation coefficient (ρ_P) is denoted for each case, and shows an overall strong correlation between $\langle \tilde{\mu}_{e,\text{blob}} \rangle$ and the blob area for all δ. Therefore, blobs with larger area tend to contain more particles, which is a straightforward reflection of equation (7).

Although a single blob with small area does not contribute much to the cross-field particle transport, it is necessary to determine whether the frequency of such small blobs counterbalances this smaller individual contribution, which would manifest as a greater density of points in figures 7(*a*)–(*d*). This is seen in figures 7(*e*)–(*h*), where the blob area is separated into equally sized bins and the bar length is the summation of data points contained in each bin. The peak of the blob area distribution tends to shift to larger blob area as δ decreases from $+0.38$ to -0.26. This means that, as δ becomes more negative, the proportion of contribution to the cross-field transport of blobs with a smaller area decreases, and that most of the blobs carrying particles radially have larger areas. In addition, as denoted in the titles of figure 7, the number of blobs detected (that cross the finish line) within 40 ms of GPI data is 327, 201, 122, and 81 for $\delta = +0.38$, $+0.15$, -0.14, and -0.26, respectively.

Furthermore, it is worthwhile to investigate whether the radial motion of blobs changes as δ changes. Figure 8 shows histograms of the time-averaged radial speed of all the blobs tracked within a 40 ms time window, not just the blobs crossing the finish line as before. The $\delta = +0.38$ case in figure 8(*a*) shows the highest mean radial blob speed ($0.50\,\text{km s}^{-1}$), whereas the $\delta = +0.15$, -0.14, and -0.26 cases in figures 8(*b*)–(*d*) show lower mean radial blob speeds (0.38, 0.41, and $0.22\,\text{km s}^{-1}$, respectively) and their distributions are skewed to lower speeds. Thus, in addition to a lower cross-field particle transport and fewer blobs, more negative δ plasmas tends to have blobs with smaller radial speed components. Also, the skewness of $\langle v_\text{r} \rangle$ is the most dramatic for $\delta = -0.26$ in figure 8(*d*), which is, again, the triangularity where first-wall interaction is suppressed, as found in [11].

Lastly, we compare the regime of the blob dynamics of these plasmas, as we have estimates of the blob sizes and speeds from the ML blob-tracking. We use the diagram presented in [7, 15] to identify the regime as in figure 9, where the four regimes are 'resistive ballooning' (*RB*), 'resistive *X*-point' (*RX*), 'connected ideal-interchange' (C_i), and 'connected sheath' (C_s). Here, Θ is a normalized blob size and Λ is a normalized plasma collisionality:

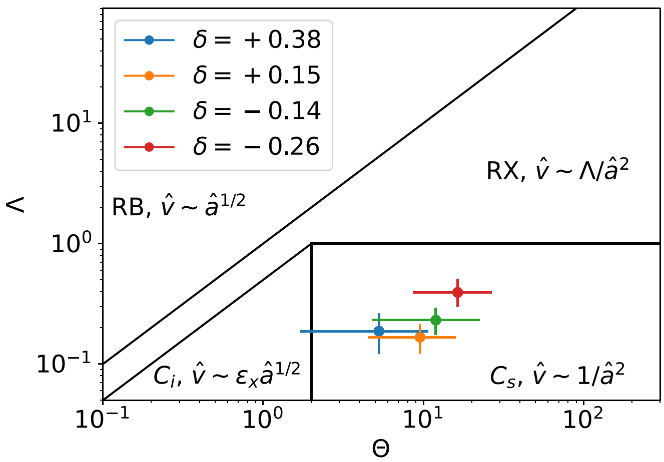

Figure 9. Diagram of Θ—Λ parameter space, where Θ and Λ are defined in equation (9). Each blob regime is indicated with the corresponding scaling of $\hat{v}$ as a function of $\hat{a}$. ϵ_x is the factor for magnetic field line fanning and approximated as $\sim$0.5 for our limited plasmas [32, 33]. The regime of plasmas with $\delta = +0.38$, $+0.15$, -0.14, and -0.26 are identified based on the average collisionality and the average size of the blobs measured by the ML blob-tracking.

$$\Theta = \hat{a}^{5/2} \quad \text{and} \quad \Lambda = 1.7 \times 10^{-18} \frac{n_e L_\parallel}{T_e^2} \tag{9}$$

where

$$\hat{a} = \frac{a_b R^{1/5}}{L_\parallel^{2/5} \rho_s^{4/5}} \quad \text{and} \quad \hat{v} = \frac{v_R}{c_s \left(2L_\parallel \frac{\rho_s^2}{R^3}\right)^{1/5}}. \tag{10}$$

a_b is the radius of blobs, $L_\parallel$ is the parallel connection length, R is the major radius, ρ_s is the ion sound Larmor radius, v_R is the radial speed of blobs, and c_s is the sound speed. In figure 9, all four cases are identified as in the C_s regime, where the filament

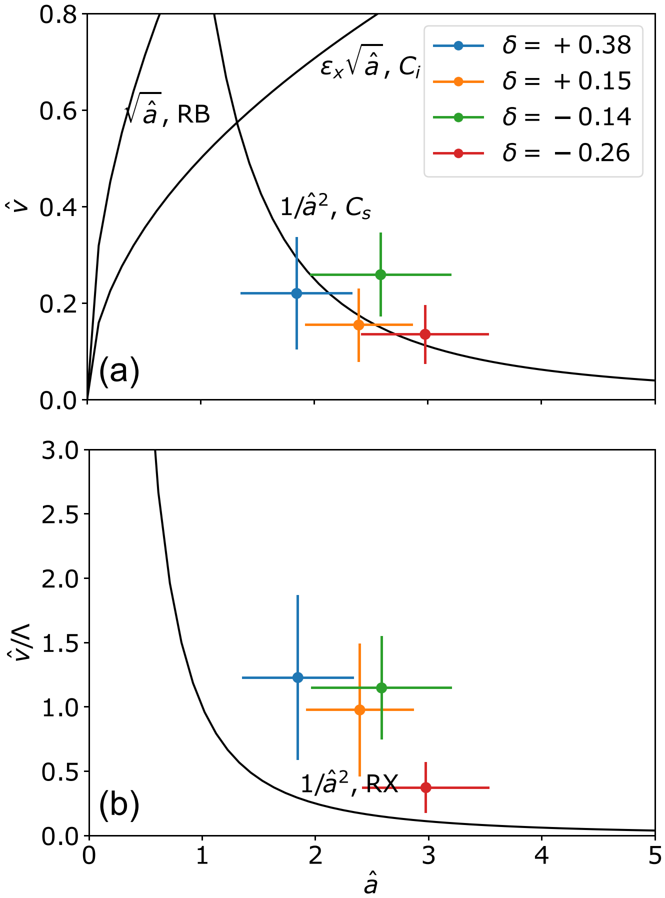

Figure 10. (*a*) $\hat{v}$—$\hat{a}$ plot with the scaling of $\hat{v}$ for *RB*, C_s, and C_i indicated. (*b*) $\hat{v}/\Lambda$—$\hat{a}$ plot with the scaling of $\hat{v}$ for *RX* indicated. The location of $\delta = +0.38$, $+0.15$, -0.14, and -0.26 cases are denoted based on the average size and speed estimation from the ML blob-tracking.

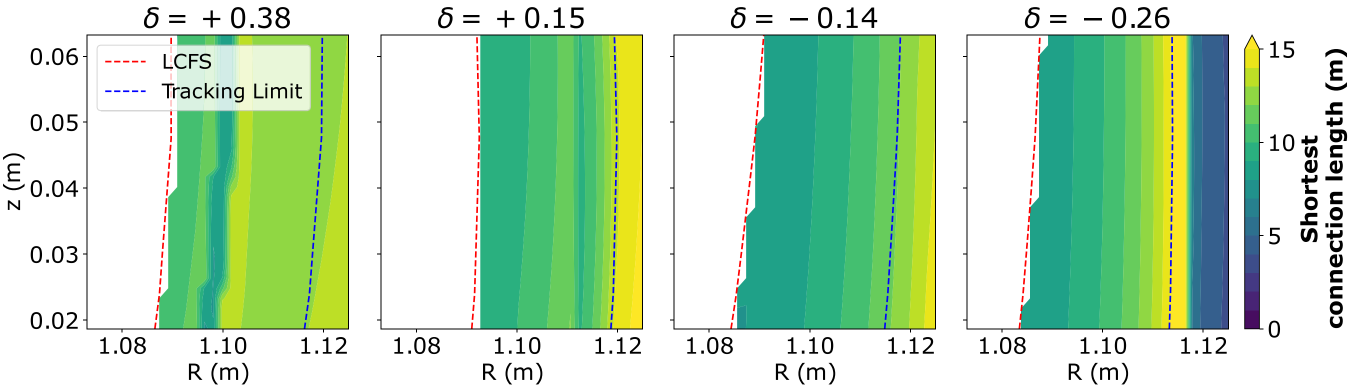

Figure 11. Shortest connection lengths from the GPI FoV for $\delta = +0.38$, $+0.15$, -0.14, and -0.26 cases. The LCFS (red) and the flux surface of the outermost limit for the blob-tracking analysis (blue) are indicated.

is electrically connected to the target sheath. In both C_s and *RX* regime, $\hat{v}$ is inversely dependent on $\hat{a}$. This is further checked by looking at the relation between $\hat{v}$ and $\hat{a}$ for the C_s and *RX* regime, as shown in figure 10. Indeed, all cases are closer to the scaling line of C_s in figure 10(*a*) than to the scaling line of *RX* in figure 10(*b*). The result in figures 9 and 10 validates the consistency of the two-region model, extending the analysis in [10] to the C_s regime in TCV.

In figure 11, the shortest connection length from the GPI FoV is shown for each δ, and the blue dashed line indicates the flux surface of the outermost limit used for the blob-tracking analysis described in section 2.2. For the $\delta = -0.26$ case, the tracking limit is located inside of where the connection length is strongly reduced which was associated with the suppression of first-wall interaction as reported in [11]. This shows that the blob radial velocity and associated transport is reduced for $\delta = -0.26$, even in regions where connection length is not reduced. The mechanism driving this behavior is currently unknown.

4. Conclusions and remarks

Cross-field particle transport at the outer midplane was estimated using ML blob-tracking in GPI image sequences and an approximate model relating D_α emission to electron density. The results so obtained are roughly consistent with those from simulations using KN1D, GBS, and SOLPS-ITER. Therefore, this type of workflow, using ML blob-tracking, is apparently able to capture those blobs that are primarily responsible for the cross-field particle transport in the far SOL. From the estimates of cross-field particle transport in plasmas with $\delta = +0.38$, $+0.15$, -0.14, and -0.26 on TCV, ML blob-tracking and KN1D give similar trends of decreasing particle flux with decreasing δ. Using the particular capability of ML blob-tracking, the contributions of blobs with different areas are explored. This analysis reveals that the reduction of cross-field particle transport in more negative δ is accompanied by a decrease in blob frequency, and that those blobs tend to have larger area and lower radial speed. Especially for $\delta = -0.26$, the low cross-field particle transport and radial blob speeds are consistent with the suppression of first-wall interaction in sufficiently negative δ, as shown in [11]. Also, the blob regime of these plasmas is the connected sheath regime and shows a velocity scaling consistent with the two-region model. This work also demonstrates the versatility of ML methods in the exploration of tokamak physics in general, and of turbulence in particular. The ML blob-tracking allows blob-by-blob analysis, providing distributions of properties derived from individual structures. Moreover, specification of the training data provides intuitive means to control algorithm performance, and allows the algorithm to replicate the outcome of a human analyst. As a future work, the method can be improved by more accurately measuring the local blob density, for example with He I line-ratio methods [34, 35] or by applying ML to GPI using He puffs [36], so that the density fluctuation in equation (7) can be directly measured without using the approximated relation with the GPI brightness in equation (6).

Acknowledgments

The authors thank F. Sciortino, A. Mathews, and S. Ahmed for invaluable suggestions. The support from the US Department of Energy, Fusion Energy Sciences, Awards DE-SC0014264 and DE-SC0020327, are gratefully acknowledged. This work was supported in part by the Swiss National Science Foundation. Also, this work has been carried out within the framework of the EUROfusion Consortium, via the Euratom Research and Training Programme (Grant Agreement No. 101052200—EUROfusion) and funded by the Swiss State Secretariat for Education, Research and Innovation (SERI). Views and opinions expressed are however those of the author(s) only and do not necessarily reflect those of the European Union, the European Commission, or SERI. Neither the European Union, nor the European Commission, nor SERI, can be held responsible for them.

ORCID iDs

W. Han https://orcid.org/0000-0002-7554-813X
N. Offeddu https://orcid.org/0000-0002-0534-1993
T. Golfinopoulos https://orcid.org/0000-0002-0898-5217
C. Theiler https://orcid.org/0000-0003-3926-1374
J.L. Terry https://orcid.org/0000-0003-4255-5509
C. Wüthrich https://orcid.org/0000-0001-7548-2452
D. Galassi https://orcid.org/0000-0003-3388-4538

References

[1] Sarazin Y. and Ghendrih P. 1998 *Phys. Plasmas* **5** 4214–28
[2] Boedo J.A. 2009 *J. Nucl. Mater.* **390–391** 29–37
[3] Krasheninnikov S.I. 2001 *Phys. Lett.* A **283** 368–70
[4] Garcia O.E., Bian N.H., Naulin V., Nielsen A.H. and Rasmussen J.J. 2005 *Phys. Plasmas* **12** 090701
[5] Zweben S.J., Boedo J.A., Grulke O., Hidalgo C., LaBombard B., Maqueda R.J., Scarin P. and Terry J.L. 2007 *Plasma Phys. Control. Fusion* **49** S1–S23
[6] D'Ippolito D.A., Myra J.R. and Krasheninnikov S.I. 2002 *Phys. Plasmas* **9** 222–33
[7] Myra J.R., Russell D.A. and D'Ippolito D.A. 2006 *Phys. Plasmas* **13** 112502
[8] D'Ippolito D.A., Myra J.R. and Zweben S.J. 2011 *Phys. Plasmas* **18** 060501
[9] Kube R., Garcia O.E., LaBombard B., Terry J.L. and Zweben S.J. 2013 *J. Nucl. Mater.* **438** S505–8
[10] Offeddu N. *et al* (The TCV Team) 2022 *Nucl. Fusion* **62** 096014
[11] Han W., Offeddu N., Golfinopoulos T., Theiler C., Tsui C.K., Boedo J.A. and Marmar E.S. (The TCV Team) 2021 *Nucl. Fusion* **61** 034003
[12] Fontana M., Porte L., Coda S. and Sauter O. (The TCV Team) 2017 *Nucl. Fusion* **58** 024002
[13] Huang Z. and Coda S. (The TCV Team) 2018 *Plasma Phys. Control. Fusion* **61** 014021
[14] Austin M.E. *et al* 2019 *Phys. Rev. Lett.* **122** 115001
[15] Myra J.R., D'Ippolito D.A., Stotler D.P., Zweben S.J., LeBlanc B.P., Menard J.E., Maqueda R.J. and Boedo J. 2006 *Phys. Plasmas* **13** 092509
[16] Han W. *et al* 2021 Exploring the edge/sol fluctuations in negative triangularity plasmas on TCV *63rd Annual Meeting of the APS Division of Plasma Physics* (Pittsburgh, PA,8 November 2021) (available at: https://meetings.aps.org/Meeting/DPP21/Session/BO07.3)
[17] Han W., Pietersen R.A., Villamor-Lora R., Beveridge M., Offeddu N., Golfinopoulos T., Theiler C., Terry J.L., Marmar E.S. and Drori I. 2022 *Sci. Rep.* **12** 18142
[18] Zweben S. *et al* 2011 *J. Nucl. Mater.* **415** S463–6
[19] LaBombard B. 2001 KN1D: a 1-D space, 2-D velocity, kinetic transport algorithm for atomic and molecular hydrogen in an ionizing plasma (available at: https://dspace.mit.edu/handle/1721.1/93211)
[20] Giacomin M., Ricci P., Coroado A., Fourestey G., Galassi D., Lanti E., Mancini D., Richart N., Stenger L. and Varini N. 2022 *J. Comput. Phys.* **463** 111294
[21] Bonnin X., Dekeyser W., Pitts R., Coster D., Voskoboynikov S. and Wiesen S. 2016 *Plasma Fusion Res.* **11** 1403102

[22] Zweben S.J., Terry J.L., Stotler D.P. and Maqueda R.J. 2017 *Rev. Sci. Instrum.* **88** 041101
[23] Offeddu N. *et al* 2022 *Rev. Sci. Instrum.* **93** 123504
[24] Cziegler I. 2011 Turbulence and transport phenomena in edge and scrape-off-layer plasmas *PhD Thesis* Massachusetts Institute of Technology (available at: https://dspace.mit.edu/handle/1721.1/77484)
[25] Zweben S.J. *et al* 2002 *Phys. Plasmas* **9** 1981–9
[26] Wüthrich C. *et al* (The TCV Team) 2022 *Nucl. Fusion* **62** 106022
[27] Sciortino F. *et al* 2020 *Nucl. Fusion* **60** 126014
[28] Dux R. 2004 *IPP Report* (Max-Planck-Institut für Plasmaphysik) (available at: https://pure.mpg.de/rest/items/item_2136655/component/file_2136654/content)
[29] Meneghini O. and Lao L. 2013 *Plasma Fusion Res.* **8** 2403009
[30] Oliveira D. *et al* (The TCV Team) 2022 *Nucl. Fusion* **62** 096001
[31] Tsui C., Boedo J., Galassi D., Loizu J., Maurizio R., Reimerdes H., Duval B., Février O., Spolaore M. and Wensing M. (The TCV Team and The Eurofusion MST1 Team) 2021 *Nucl. Fusion* **61** 046004
[32] Tsui C.K. *et al* 2018 *Phys. Plasmas* **25** 072506
[33] Myra J.R., D'Ippolito D.A., Xu X.Q. and Cohen R.H. 2000 *Phys. Plasmas* **7** 4622–31
[34] Linehan B. *et al* (The TCV Team) 2023 *Nucl. Fusion* **63** 036021
[35] Griener M., Wolfrum E., Cavedon M., Dux R., Rohde V., Sochor M., Muñoz Burgos J.M., Schmitz O. and Stroth U. 2018 *Rev. Sci. Instrum.* **89** 10D102
[36] Mathews A., Hughes J.W., Terry J.L. and Baek S.G. 2022 *Phys. Rev. Lett.* **129** 235002